Chapter 2

Laser Stabilization and Dissemination for Strontium Optical Clocks

Qiushuo Sun, Jonathan M. Jones, Alok Singh, Abhilash Jha, Markus Gellesch, Yogeshwar Kale, Vijay Singh, Richard Barron, Manan Jain, Kai Bongs and Yeshpal Singh

2.1. Introduction

Precision timing is the key that enables a wide range of modern techniques, including satellite-free navigation, broadband communication, and relativistic geodesy [1, 2]. Microwave frequency atomic clocks are commercially available and are commonly used as accurate timing references, with the best primary standards achieving fractional frequency uncertainties of 1.6 parts in 10^{16} [1]. Optical atomic clocks use the frequencies of visible lights as reference; they have the potential to improve the clock performance by a factor of at least 100 [1]. As one of the most precise atomic clocks so far, strontium (Sr) optical lattice clocks have reached 10^{-18} fractional frequency uncertainty [2], achieved by referencing an ultra-stable laser to the millihertz-linewidth $^1S_0$-$^3P_0$ transition in strontium atoms.

Laser cooling method is used to acquire cold atoms in optical clocks. To provide the sufficient confinement to the atoms, the laser cooling processes take place in a vacuum chamber with a spatially dependent magnetic field, this is commonly referred to as a magneto-optical trap (MOT). In Sr clocks, the atoms are primarily collected and cooled down to a few mK from hot Sr vapor source by the first stage laser cooling, then the photon-recoil-limited temperatures below 1 μK are reached by the second stage of narrow line Doppler cooling [3]. The second stage cooling laser is also referred to as the 'red MOT laser' and has an output

Qiushuo Sun
School of Physics and Astronomy, University of Birmingham, Birmingham, UK

of 689 nm (434 THz, Fig. 2.1). As the natural width of the $^1S_0$-$^3P_1$ transition is 7.5 kHz, the linewidth of the red MOT laser needs to be relatively small and is usually below 1 kHz. Compared to ^{88}Sr, ^{87}Sr requires two more outputs at 689 nm: stirring beam and polarizing beam, they help provide population randomization in the second stage cooling and the desired frequencies are both close to the frequency of the red MOT laser, as shown in Fig. 2.1 [4].

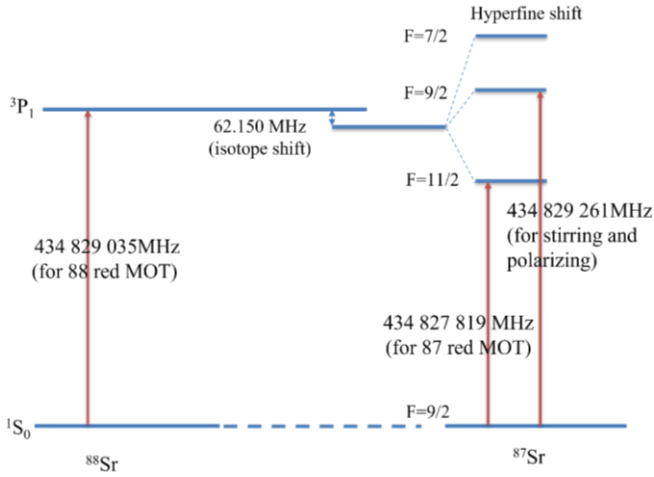

Fig. 2.1. The energy level scheme for ^{87}Sr and ^{88}Sr red MOT. The frequencies in the figure are the locking points of the lasers, they are shifted to the atom transition frequencies by acousto-optic modulators (not shown here).

The 'clock laser' is an ultra-stable, narrow linewidth laser with a 698 nm output that is used to probe the sub hertz-linewidth $^1S_0$-$^3P_0$ transition of Sr atoms. The stability and linewidth of this laser determine the performance of the optical atomic clock, especially at short measurement durations (or high Fourier frequencies). The linewidth of this laser needs to be reduced to below 10 Hz for Sr clock spectroscopy measurements.

A free-running laser can have the linewidth up to few MHz. In this chapter, the Pound-Drever-Hall (PDH) laser locking technique and phase-offset locking technique are elaborated and experimentally developed to narrow the linewidth of the red MOT lasers and clock lasers for Sr optical clocks. The stabilization results are characterized by either beating the locked laser against another stable laser or using the locked laser to engage the second stage red MOT cooling.

These ultra-stable lasers are not as transportable as other lasers due to the complexity of systems as well as highly fragile cavities for laser stabilization. To transfer the narrow-linewidth lights from one place to another, a polarization-maintaining optical fiber represents a nearly ideal transmission medium. To maintain the frequency stabilization of the light, the noise induced by the fiber needs to be cancelled out. In this Chapter, we also present the fiber noise cancellation setup for the precise dissemination of the ultra-stable lasers.

2.2. Methods and Results

2.2.1. Lasers and Light Distribution

Fig. 2.2 demonstrates the laser stabilization solutions in the two labs at the University of Birmingham (UoB). Two lab-constructed external cavity diode lasers (ECDL) operating at 698 nm were used as the clock lasers, one was stabilized by a vertical cavity (V cavity) and the other was locked to a horizontal cavity (H cavity). This will be elaborated in Section 2.2.2.2. A commercial 1396 nm sub-hertz linewidth laser (MENLO GmbH) was used to calibrate the clock laser in Lab 1. Two ECDLs operating at 689 nm provided sufficient power for the red MOT, polarizing, and stirring beams for ^{88}Sr and ^{87}Sr atoms; the master laser was locked to the horizontal cavity, and the slave laser was phase-offset locked to the master laser. The rest of the lasers in Lab 2 for Sr clocks including 461 nm blue MOT and Zeeman slower laser, 679 nm and 707 nm repumped lasers, had a linewidth requirement at MHz level, they were locked to the Wavelength Meter from HighFinesse GmbH. A 100-meter-long fiber connection was built between the two labs for future communications.

Both 698 nm lasers and both 689 nm lasers in Fig. 2.2 were lab constructed ECDL in Littrow configuration, Fig. 2.3 (a) shows the typical schematic. The anti-reflection coated laser diodes SAL-0690-025 (689 nm) and SAL-0705-020 (698 nm) were purchased from Sacher Lasertechnik GmbH, with a maximum output power of around 40 mW. The grating and the laser diode formed the external cavity, the grating (1800 lines per millimeter) was mounted to a piezo actuator, enabling a ~5 GHz tuning range in the output wavelength, as highlighted in Fig. 2.3 (b). The beam output the laser cavity box from the wedged window, the wedged shape was to avoid any etalon effect. The 35 dB

isolator stopped any retroreflective beam going back to the laser diode to cause any future issues. After passing through the half waveplate and polarized beam splitter (PBS), the output beam was linear polarized.

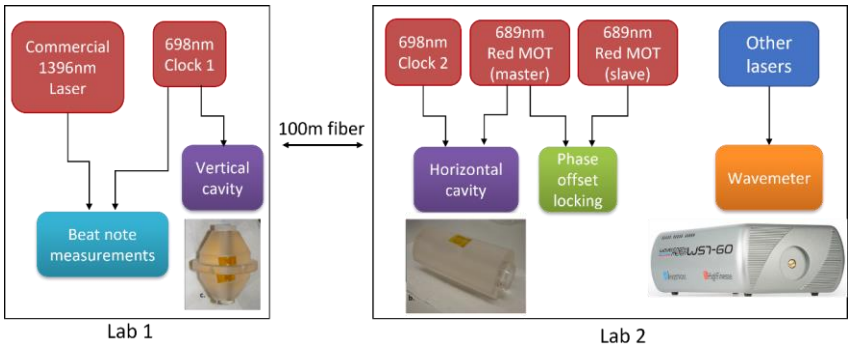

Fig. 2.2. The laser stabilization in two labs at the UoB for strontium cold atom experiments.

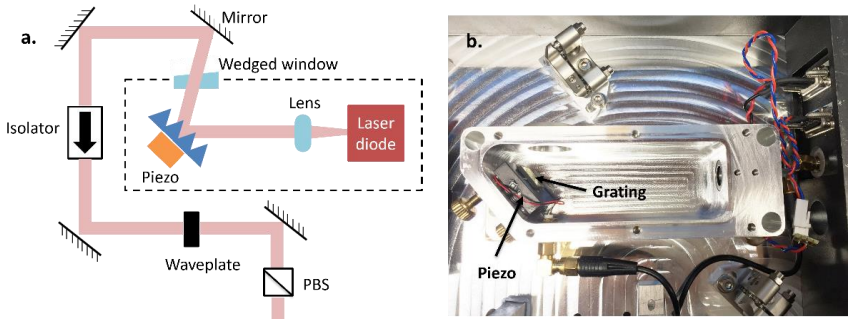

Fig. 2.3. (a) Schematic of the lab constructed ECDL in Littrow configuration. (b) A photo of inside of the laser box, highlighting the grating and piezo.

To engage the stabilization, each ECDL was equipped with a temperature controller, a current driver, and a piezo controller. It was essential that the current controller had a high-bandwidth modulation input (> 5 MHz) to receive the feedback from the locking servo. The piezo controller enabled the slow loop locking, avoiding the laser drift over a long-time scale. The controllers used in this study were DCC110 and DTC110 from TOPTICA Photonics, D2-105 from Vescent Photonics, TEC100L and DRV200S from Koheron.

Fig. 2.4 illustrates the experimental setup of the two lasers in Lab 1. The lab-constructed 698 nm laser was stabilized to the V cavity by the PDH locking method, as highlighted in the blue dashed box. The commercial laser had an output wavelength of 1396 nm, it was converted to 698 nm by a frequency doubling crystal to compare against the lab constructed clock laser. This laser was quoted with sub-Hertz linewidth, but the true linewidth remained unknown. The beams from the two lasers were merged by a PBS, the polarization directions of the beams on the photodetector were consistent after passing the polarizer, giving a beat note signal to evaluate on the spectrum analyzer. The acousto-optic modulator (AOM) enabled the accurate frequency control and fast on/off control of the beams.

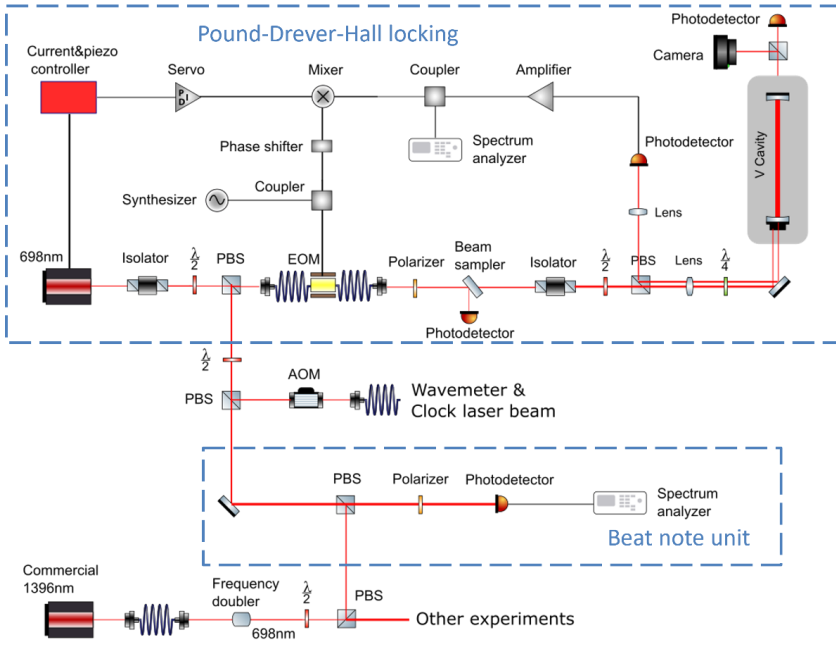

Fig. 2.4. Experimental setup of the lab-constructed 698 nm laser and the commercial 1396 nm laser in Lab 1. It was drawn using the optics toolbox published in [5]. The two dashed boxes highlight the PDH locking setup and the beat note detection unit.

The experimental setup of the light distribution of 698 nm laser and two 689 nm lasers in Lab 2 is shown in Fig. 2.5. Both 698 nm and 689 nm master lasers were stabilized by the H cavity, the beams were combined

by a 50:50 beam splitter. The 689 nm slave laser was phase-offset locked to the master laser with a fixed offset frequency, this is elaborated in Section 2.2.3. The output of the 698 nm laser and three outputs of the 689 nm lasers were sent to the cold atom physics package, the 689 nm master laser provided the red MOT beam for the second stage cooling of the atoms, the stirring beams and polarizing beams for ^{87}Sr atoms were supplied by the slave laser.

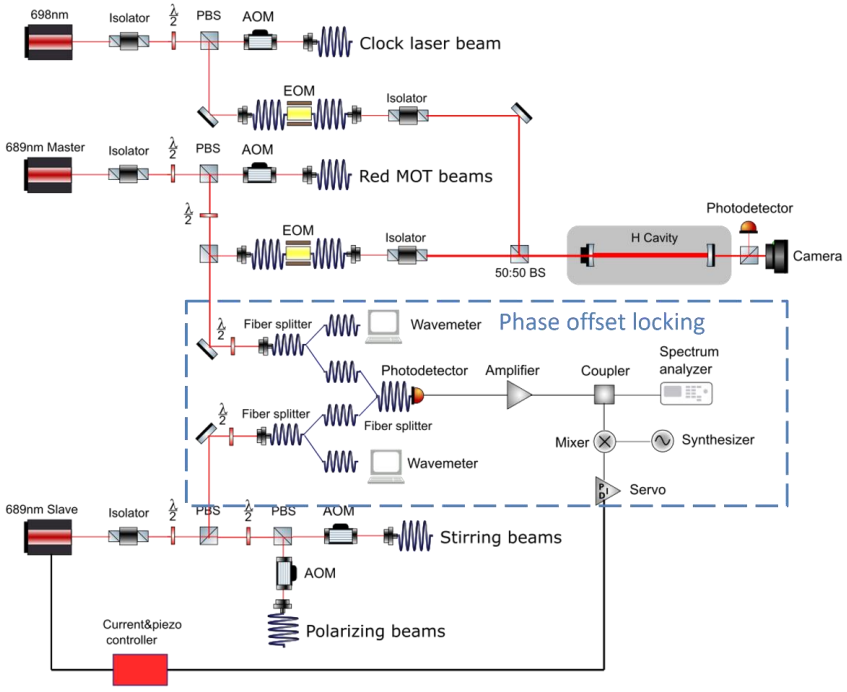

Fig. 2.5. Experimental arrangements of 698 nm laser and two 689 nm lasers in Lab 2. The blue dashed box shows the setup of the phase offset locking between two 689 nm lasers. Some components in the PDH locking setups for 698 nm and 689 nm master laser are not shown.

2.2.2. Pound-Drever-Hall Locking

The Pound-Drever-Hall technique (PDH) was proposed in 1983 [6] and has been widely used as a laser locking method, given that the cavity is well stabilized at appropriate temperature and under certain vacuum environment, as well as is kept from the low frequency vibrations. The

frequency of the laser is stabilized by a Fabry-Perot reference cavity that consists of a spacer and two mirrors. The phase-modulated laser beam is sent into the cavity from one of the mirrors, forming a standing wave resonance inside the cavity if a half integer multiple of the wavelength of the incident beam equals to the distance between the mirrors. The reflected beam is captured by a photodetector, generating an optical heterodyne signal between the carrier frequency and sidebands. By mixing this signal with the modulating signal, a correction signal is generated and feedbacked to the laser to stop it from drifting. PDH locking technique has been proved to be highly effective and has achieved laser linewidths below 40 mHz [7].

2.2.2.1. Experimental Setups

The blue dashed box in Fig. 2.4 presents a typical schematic of the PDH locking technique. The RF phase modulation of the beam was engaged by an electro-optical modulator (EOM), the details are given in Section 2.2.2.3. After the EOM, any polarization fluctuation was filtered out by a high extinction ratio polarizer. An optical isolator at >30 dB was placed before the cavity, together with the isolator inside the laser box, the laser diode was protected from any retroreflective beams by a total of >65 dB isolation. The beam sampler picked off a small percentage of the light to go to the photodetector, to double check the power fluctuation. The beam was incident into the cavity from the planar mirror, the reflected light from the cavity was captured by a high-speed detector (PDA10A2 from Thorlabs, bandwidth 150 MHz). The signal was amplified by the low phase noise amplifier, and then was demodulated by mixing with the phase-shifted RF modulation signal. FALC 110 from TOPTICA Photonics was used as the locking servo, the slow branch was feedbacked to the laser piezo controller and the fast loop output was connected to the fast modulation input on the current driver.

2.2.2.2. Cavities

2.2.2.2.1. Design and Assembly

Two cavities were used in this study. The vertical cavity (V cavity) was designed by NIST, it was used to stabilize the external cavity diode lasers and achieved a 0.5 Hz linewidth [8]. The horizontal cavity (H cavity) was similar to the NPL design [9] and has been used by different research

groups. The spacers of both cavities are made of Corning ultra-low expansion (ULE) material and the mirrors are made of fused silica; they were assembled via optical contact bonding. All the mirrors have the high reflectivity dielectric coatings specially designed for 698 nm on the inner side and anti-reflection coatings on the outer side. The photos of the V and H cavities are shown in Fig. 2.6. Each cavity has a planar mirror and a curved mirror with a radius of curvature of 1 m [10].

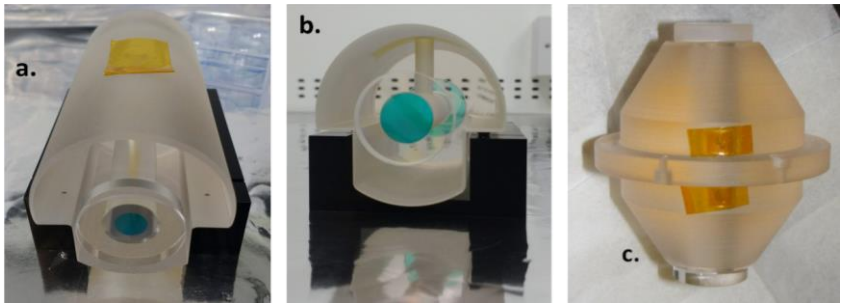

Fig. 2.6. (a-b) Photos of horizontal cavity, (c) Vertical cavity. (c) is adapted from [10].

Table 2.1 gives the details of two cavities. The length of the spacer in the V cavity is 77.5 mm, and 100 mm of that in the H cavity. The free spectral range of the cavity is calculated by:

$$FSR = \frac{c}{2L}, \tag{2.1}$$

where c is the speed of light, L is the distance between the mirrors.

Table 2.1. Parameters of two cavities.

	Design	**Length (mm)**	**Free Spectral Range (GHz)**	**Pressure (mbar)**	**Temperature (°C)**	**Vibration Cancellation**
Vertical cavity	NIST [8]	77.5	1.9	1.7×10^{-7}	16	Minus K Technology 100BM-8
Horizontal cavity	NPL [9]	100	1.5	1.8×10^{-10}	10	Table Stable AVI-200M/LP

The total thermal noise of the H cavity was numerically calculated as $3.73\times10^{-17}\ Hz/\sqrt{Hz}$ at a frequency of 1 Hz, including 3.3 % Brownian noise of the mirrors, 53.4 % Brownian noise of the coatings, 25.3 %

Brownian noise of the spacer, 18.0 % thermoelastic noise, and neglectable amount of photothermal noise [10]. As both cavities are made of the same materials and have similar shape and length, the thermal noise of V cavity was estimated to be close to that of the H cavity.

2.2.2.2.2. Stability Control

The stability of the cavity directly determines the performance of the laser. When the optical path distance between the mirrors is stable, a robust reference can be formed, and hence a good performance in the laser stability. To achieve this, the cavity should be kept in an enclosed environment to avoid any possible vibrations or temperature fluctuation.

Vibration isolation platforms can largely reduce the susceptibility of cavities to vibrations from the environment. The vacuum chamber of the V cavity and light distribution bread board were mounted on a 100BM-8 platform from Minus K Technology. The H cavity system and optical bread board were placed on top of AVI-200M/LP platform from Table Stable. Both cavities were carefully supported from the bottom using specially designed supporting base and Viton balls [10].

Air flow inside the cavity causes changes in the refractive index of the medium, leading to the changes in the optical length. Consequently, cavities usually operate in a vacuum environment with a pressure below 10^{-7} mbar. In this study, both vacuum chambers were connected to an ion pump to keep a low pressure. The V cavity had a pressure of 1.7×10^{-7} mbar and the H cavity had a pressure of 1.8×10^{-10} mbar. The pictures of the vacuum systems are shown in Fig. 2.7.

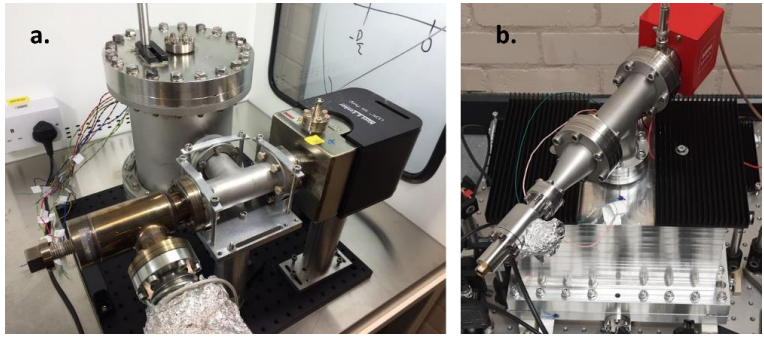

Fig. 2.7. Photos of the vacuum systems for (a) vertical cavity, and (b) horizontal cavity.

2.2.2.2.3. Temperature Control

Due to the large volume and the long integration time constant of cavity systems, digital temperature controllers are preferred over analog controllers. The digital temperature controller used in this work was designed and programmed by Dr Charles Baynham, the details can be found in [11].

Fig. 2.8 shows the schematic of the temperature control of the vacuum chamber systems for the cavities. The V cavity chamber was mostly constructed from 316 stainless steel, with the bottom flange constructed from aluminum to aid with heat removal from the in-vacuum temperature control elements. There were two aluminum layers inside each chamber, the outer layer was connected to the Peltier elements to actively control the temperature, whilst the inner layer passively isolated the temperature. The thermistors were attached to both aluminum layers in the chamber for the V cavity. A total of three Peltier elements were glued between the outer aluminum layer and the titanium chamber, they were connected in parallel configuration and were controlled by a channel in the temperature controller. The heat sinks were fixed at the bottom of the chamber to help evacuate heat. Due to the limitation of the heat dissipation, the temperature of this cavity was kept at 16 °C.

The H cavity chamber was constructed from aluminum and sealed using a combination of indium and CF fittings. This aluminum chamber acted not only as a pressure vessel but also as a first active stage of temperature control, limited by the dew point of the laboratory. Within the vacuum chamber, the cavity was mounted within a passive heat shield layer constructed from aluminum. This passive layer was separated from the active layer by fuse silica balls which have a low thermal conductive, providing point-like contact which further minimizing thermal conduction. The in-vacuum aluminum temperature-controlled elements contain steeply angled venting holes allowing gasses to be pumped effectively whilst minimizing line of sight between the cavity and parts of the chamber at different temperatures. In the vacuum chamber of the H cavity, the thermistors were placed on the outer aluminum layer next to the Peltier elements, as well as on the outside of the vacuum chamber. Temperature sensors were not present on the inner passive heat shield, to remove the potential for heat conduction and the need for cable feed throughs on the heat shields. The Peltier elements underneath the chamber transferred the heat to the breadboard, the ones at the top were attached to the heat sinks to dissipate heat. These Peltier elements were

in parallel configuration and controlled by 4 separate channels in the temperature controller. The temperature of the cavity was kept at around 10 °C, the temperature of the vacuum chamber was at 17 °C. To help stabilize such a low temperature, the vacuum chamber was surrounded by a plastic box made of Acrylic (Perspex®) Sheets, the material has a thermal conductivity of below 0.2 W/mK at 25 ˚C. The whole PDH system was isolated from the room by a box made of acoustic foams and cardboards.

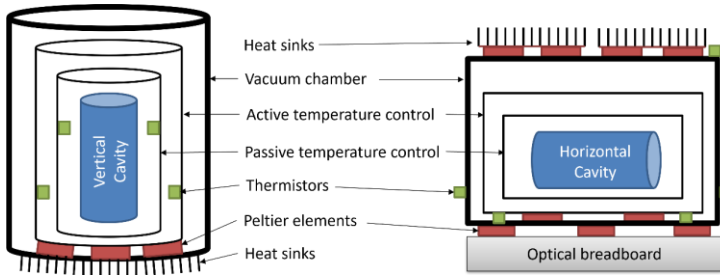

Fig. 2.8. Schematic of temperature control for the cavity systems, green boxes indicate the thermistors, red boxes indicate the Peltier elements.

We characterized the performance of the digital temperature controller by measuring the temperature fluctuation in the V cavity and calculating Allan deviation, the results are shown in Fig. 2.9. After stabilization, sigma-tau plots show that the inner layer has a variation below 1×10^{-4} K, indicating an even lower temperature fluctuation on the cavity itself.

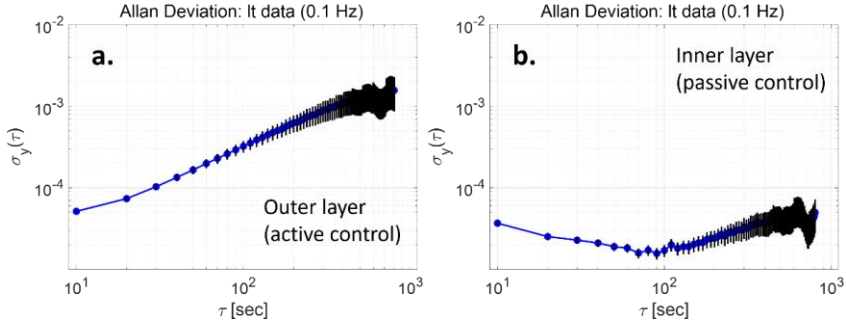

Fig. 2.9. Allan deviation of the temperature fluctuation within 1 hour in the V cavity. (a) The outer aluminum shield result, (b) the inner aluminum layer results.

2.2.2.2.4. Mode Matching

To maximize the light coupling efficiency, the waist of the incoming beam at the input mirror should be equal to the cavity waist, this is usually referred to as cavity mode matching and can be achieved by optical lenses. The radius of a Gaussian beam propagating along *z* axis can be calculated by:

$$w(z) = w_0\sqrt{1 + (z/z_R)^2}, \tag{2.2}$$

with the Rayleigh length:

$$z_R = \frac{\pi w_0^2}{\lambda}, \tag{2.3}$$

where w_0 is the beam radius at the beam waist, λ is the wavelength. The beam radii along x and y axes at varies distance before entering the cavity were measured with a beam profiler. All reasonable combinations of the beam waist w_0 and its location z_0 were enumerated and substituted into Equation (2.2) to calculate the beam radii at different *z* values, the results were compared with the measured data to find the local minima. Fig. 2.10 plots the fitting results.

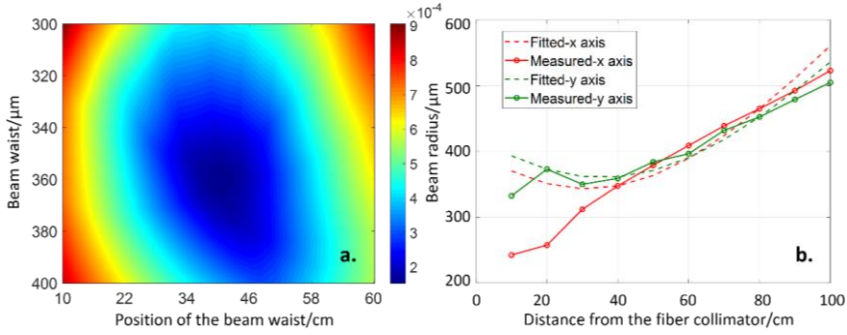

Fig. 2.10. (a) The difference between the sum of the calculated beam radii when assuming varies beam waist and waist position and the sum of the measured beam radii at same positions. The blue color indicates a good match whilst the red color means a bad guess. The local minima were found at beam waist 343 μm along *x* axis and 360 μm along *y* axis. (b) Measured Gaussian beam propagation profile and the calculated one using the local minima results in (a).

As shown in Fig. 2.10 (a), when the beam waist along *x* axis w_{0x} = 343 μm, the beam waist along *y* axis w_{0y} = 360 μm, the position of the waist along *x* axis z_{0x} = 315 mm (z_0 = 0 at the fiber collimator output), and the position of the waist along *y* axis z_{0y} = 356 mm, the local minima was reached. Using these values to calculate the Gaussian propagation profile, the fitted results matched well with the measured ones, as shown in Fig. 2.10 (b).

Knowing the beam waist and the position of the waist, a single lens can be added to the beam path for the mode matching under certain constrains of input waist, cavity waist and optical path length. The position and focal length of the lens were calculated by the Equations (9, 10, 16) in [12].

2.2.2.2.5. Finesse Measurements

The finesse of both V and H cavities were quoted to be 400000 and measured to be 385000 and 337000, respectively [10]. The aging of the cavities over the years, as well as the reassembly led to a reduced finesse. The ring-down measurement was performed on both cavities: after quickly shutting down the light source, the time constant τ of the decay rate of the dissipated energy from the cavity was captured to extract the finesse. The decay rate of transmitted light intensity can be written as:

$$I(t) = I_0 e^{-t/\tau}, \tag{2.4}$$

where I_0 is the transmitted intensity on the photodetector when the laser is locked, *t* is the decay time. The finesse can be calculated by [13]:

$$\mathcal{F} = \frac{c\pi\tau}{L} \tag{2.5}$$

The schematic of the ring-down measurement is shown in Fig. 2.11(a). A quick-response RF switch was used to turn on and off the servo output to the laser current controller, it was controlled by a squared trigger signal. When the trigger signal was on, the servo feedback to the laser current driver was blocked by the RF switch, the laser was unlocked and shifted away from the TEM00 mode, the intensity decay of the transmitted light was captured by the photodetector, as shown in Fig. 2.11 (b). The fitted decay constant τ was 18.5 μs for the V cavity. Using Eqn. (2.4), the finesse was calculated to be ~226784. Similarly, a finesse of ~150000 was calculated for the H cavity.

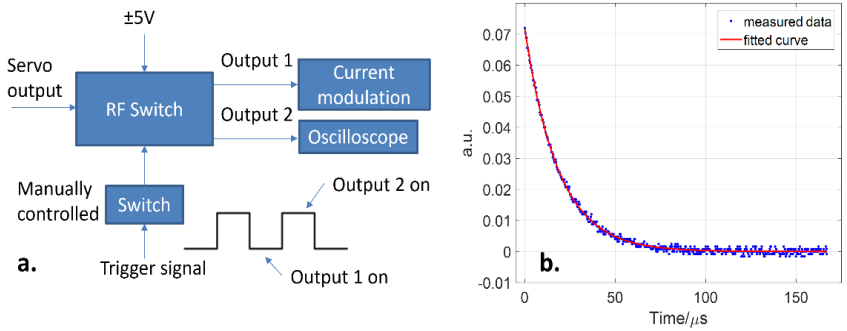

Fig. 2.11. (a) The schematic of the ring-down measurement for cavity finesse calculation. (b) An example of the ring-down measurement result, the fitted decay constant τ is 18.5 μs.

2.2.2.3. Electro-optical Modulator

PM705, a fiber-coupled electro-optical modulator (EOM) from Jenoptik AG was used to modulate the phase of the laser beam and generate the sidebands. It has a spectral bandwidth of ±20 nm and an insertion loss of 5 dB. The RF signal applied onto the EOM varied from 10-40 MHz for different locking setups. A half waveplate was used before the EOM to enable careful alignment of the beam polarization direction to the fiber axis to reduce the residual amplitude modulation. When an external electric field is applied, the refractive index of the Lithium niobate ($LiNbO_3$) crystal in the EOM changes proportionally to the electric field strength, its direction, and the polarization of the light. The EOM modulated signal can be written as:

$$V_m = V_c cos\left[\omega_c t + \beta \cos(\omega_\beta t)\right], \tag{2.6}$$

where V_c is the amplitude of the carrier signal, ω_c is the angular frequency of the input beam, ω_β is the frequency of the modulated signal. The modulation index β can be calculated by:

$$\beta = \frac{V_p}{V_\pi} \times \pi, \tag{2.7}$$

where V_p is the peak voltage of the applied RF signal, V_π is the half wave voltage of the EOM. The amplitude of the modulated signal with sidebands follows the Bessel function:

$$J_n(\beta) = \left(\frac{\beta}{2}\right)^n \left[\frac{1}{n!} - \frac{\left(\frac{\beta}{2}\right)^2}{1!(n+1)!} + \frac{\left(\frac{\beta}{2}\right)^4}{2!(n+2)!} - \frac{\left(\frac{\beta}{2}\right)^6}{3!(n+3)!} + \cdots\right], \quad (2.8)$$

where ! is the factorial and n is the number of the side frequency. Fig. 2.12 below plots the calculated the intensity ratio between the sidebands and zero order with various modulation indices when $V_\pi = 5$ V. When the modulation index $\beta = 1.41$, the intensity of the first order sidebands is equal to the intensity of the carrier signal. In this work, the intensity of each sideband was roughly half of the power ($\beta = 1.08$) in the carrier signal, as it gave the maximized slope of the error signal [14].

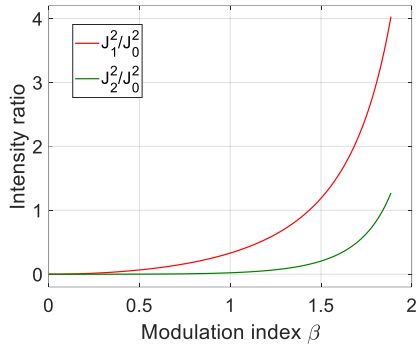

Fig. 2.12. After modulation, the intensity ratio between the first order and zero order (red), second order and zero order (green), changes with modulation index, assuming $V_\pi = 5$V.

2.2.2.4. Locking

To lock the laser, the laser frequency was tuned close to the desired value by adjusting the diode temperature and current, a triangular signal was applied onto the piezo controller to scan the output wavelength of the laser and observe the transverse modes on the camera. The high-order modes were transmitted through and cavity and observed at the beginning, adjusting the two mirrors before the cavity to optimize the lowest mode visible on the camera, a lower order mode would appear. Repeatedly locating the lowest mode and optimizing the alignment, eventually TEM00 mode was observed and its brightness could be optimized. Fig. 2.13(a) shows the time-domain error signal when the laser was scanned across the TEM00 mode, the carrier signal and the

sidebands were observed, as highlighted in the figure. Fig. 2.13(b) is the image on the camera when the laser was locked, the transmitted power was 15 % of the input power to the cavity. Fig. 2.13(c) shows the coupler signal detected on the spectrum analyzer when the laser was locked to TEM00 mode, indicating a servo loop bandwidth of 500 kHz.

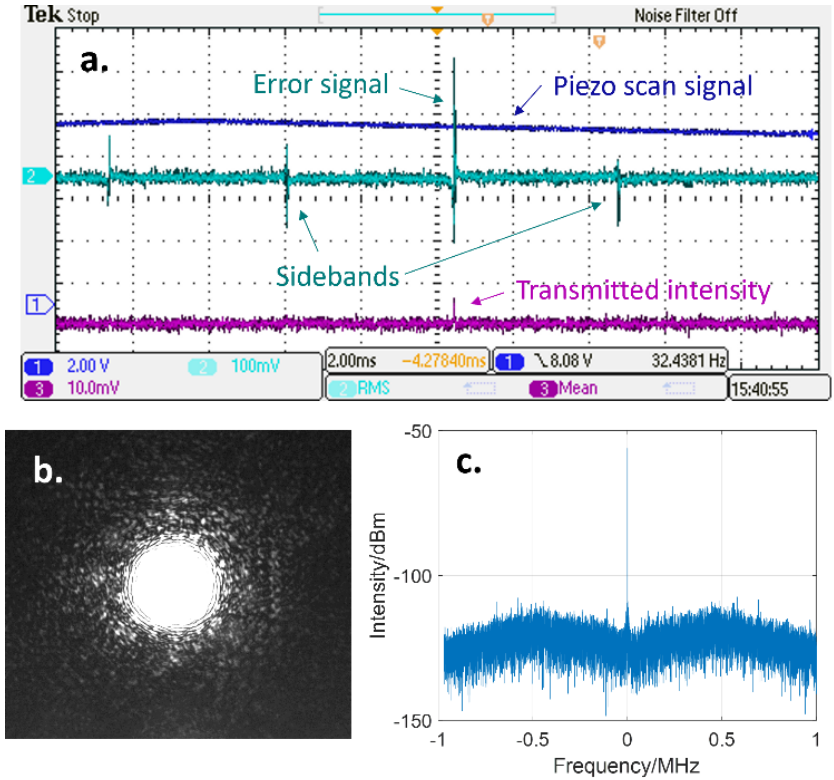

Fig. 2.13. (a) The error signal on the oscilloscope when the laser was scanned across TEM00 mode, deep blue is the triangular piezo scan signal, cyan data is the time-domain error signal, and the purple curve is the transmitted signal on the detector. (b) The bright TEM00 mode captured on the camera when the laser was locked. (c) The signal on the spectrum analyzer when the laser was locked.

An AOM is commonly used to shift the frequency of the locked beam to the desired frequency. Alternatively, dual sideband locking method was applied in this work. The RF signal at a fixed frequency was sent to the EOM to generate the first set of sidebands for the PDH locking,

additionally, a broadband signal at around 600 MHz was sent to the termination input of the fiber-coupled EOM to impose a second set of sidebands on the carrier, this set of sidebands was tunable and acted functionally as the laser carrier for the other set of sidebands [15]. The laser was locked at 600 MHz away from the original TEM00 mode.

2.2.2.5. Linewidth Characterization

As no electronics are fast enough to measure the frequency of visible light with such accuracy, two separate laser and cavity setups are required to characterize the linewidth of the laser. The beat note, which is the frequency difference between the two lasers that are stabilized by two cavities, can be captured and analyzed, the results give a good indication of the laser linewidth.

The 698 nm clock laser in Lab 1 was characterized by beating it against the commercial ultra-stable laser, the setup is shown in Fig. 2.4. The beat note signal was measured by a spectrum analyzer, the center frequency was at 39.1 MHz, this was the frequency difference between the two lasers. Fig. 2.14 presents the measured signal when the resolution bandwidth of the spectrum analyzer was 5 Hz; the extracted linewidth from the Gaussian fitting of 8 beat note signals was 161±50 Hz. This linewidth was assumed to be the linewidths of the two lasers added in quadrature.

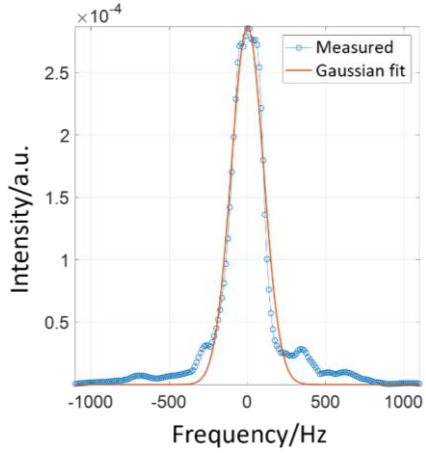

Fig. 2.14. (a) The measured beat note on the spectrum analyzer and the Gaussian fit on the beat note signal.

The performance of the horizontal cavity in Lab 2 was characterized by sending the stabilized lasers to the physics package and attempting the second stage cooling. To acquire the broadband red MOT, the modulation depth of 1 MHz with modulation frequency of 25 kHz was applied to the red MOT beam. The transfer efficiency of cold atoms from the first stage cooling (blue MOT) to the narrow-line cooling (broadband red MOT) was ~35 %. Fig. 2.15 (a) shows the broadband red MOT result, the colormap is the detected density of the atom cloud, the two curves are the fitted atom density along x and y axis. The calculated atom number in the broadband red MOT was 2.11×10^6.

The time-of-flight (ToF) measurements have been performed to estimate the temperature of the cloud (Fig. 2.15(b)). The expanding MOT cloud size σ (Gaussian radius width) and flight time t were related to temperature (T) by $\sigma^2(t) = \sigma_0^2 + (k_B T t^2/m)$, where σ_0 is the cloud size at zero time of flight, k_B is Boltzmann constant, m is the atomic mass of ^{88}Sr. The square of the size of broadband red MOT was plotted as a function of the square of the flight time. Typically 2×10^6 atoms were trapped at ~ 10 μK in the broadband red MOT.

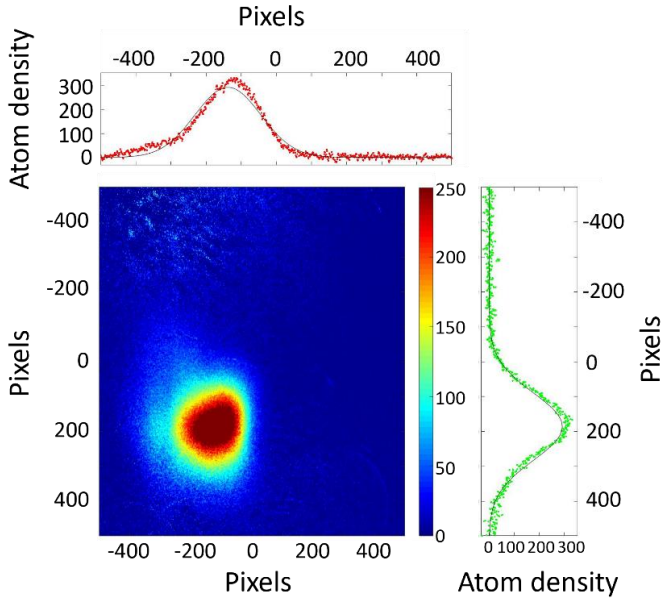

Fig. 2.15 (a). Broadband red MOT with experimental parameters. A pixel is 6.45 μm.

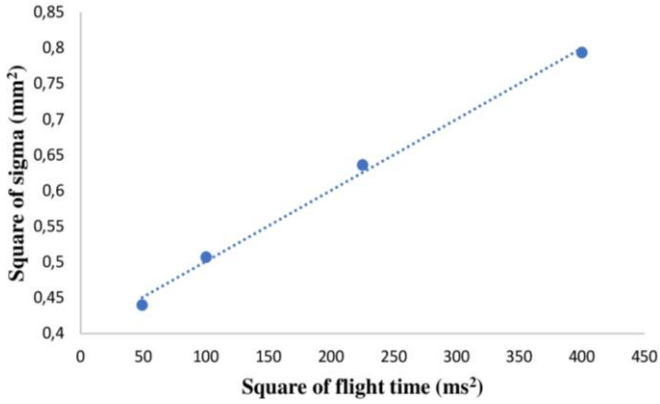

Fig. 2.15 (b). Time-of-flight measurement result of the broadband red MOT.

2.2.3. Phase Offset Locking

Stabilizing a laser to a cavity is highly effective but also costly and high maintenance. Alternatively, offset-locking a laser to another frequency stabilized laser is more straightforward if the beat note frequency between these two lasers is within the bandwidth of the photodetector. Additionally, in the experiments of Sr optical clocks, offset locking facilitates the fast switching between the trapping of ^{87}Sr and ^{88}Sr atoms [4]. Compared to the frequency locking method between two lasers, phase locking is more complicated, but the achievable frequency stability is a lot higher [16].

Fig. 2.5 shows the schematic of the phase offset locking between two 689 nm lasers. The beams from the master and slave lasers were combined by three fiber splitters, the outputs provided a separating beam for each laser going to the wavemeter to monitor the wavelength. The beat note signal between the two lasers was at 1.44 GHz and was measured by a high-speed photodetector. The amplified signal was mixed with the 1.44 GHz RF signal, the generated error signal was sent to the PID servo (FLAC 110 from TOPTICA Photonics) and then feedbacked to the controllers of the slave laser. This setup allowed the output frequency of the slave laser followed the frequency of the master laser with a fixed offset of 1.44 GHz. When the offset locking was engaged, the coupler signal measured on the spectrum analyzer is shown in Fig. 2.16. The humps are 600 kHz away from the main peak, indicating a good locking loop bandwidth. The phase-locked 689 nm

laser will provide the stirring beams and the polarizing beams for ^{87}Sr clock.

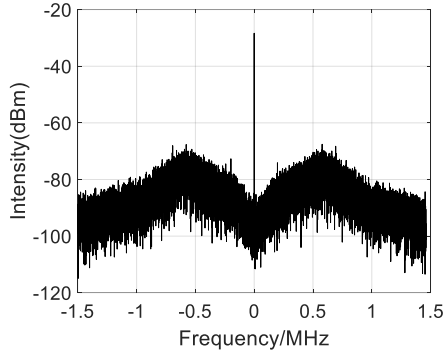

Fig. 2.16. The phase offset locking loop had a bandwidth of 600 kHz. The center frequency was shifted by 1.44 GHz.

2.2.4. Fiber Noise Cancellation

To reduce the effect of the long fibers, the fiber noise cancellation setup was developed following the schematic in Fig. 2.17. The output frequency of the pre-stabilized laser was f_l. An RF signal at $f_{AOM} + f_{reg}$ was sent to the AOM and the first order output was sent into a long fiber. A small amount of the light was reflected back to the fiber by the beam sampler, in this process the fiber noise induced frequency shift f_n was added twice to the laser frequency. The frequency after double passing the AOM and the long fiber was $f_l + 2(f_{AOM} + f_{reg} + f_n)$, beating this signal with the signal from the other arm of the interferometry at frequency f_l, an electrical signal with $2(f_{AOM} + f_{reg} + f_n)$ frequency was acquired on the photodetector. This photodetector signal was then demodulated by the $2f_{AOM}$ RF signal, the PID servo and the direct digital synthesizer (DDS) controlled the value of the regulating frequency f_{reg} to be equal to f_n, and output $f_{AOM} + f_{reg}$ to the AOM. The synthesizer for the $2f_{AOM}$ signal used was a 156 MHz crystal oscillator (ABRACON/ABLNO-V-156.250 MHz), PID servo was LB1005 High-Speed Servo Controller from Newport, the DDS was AD9912 from Analog Devices [17]. Fig. 2.18 demonstrates the coupler signal on the spectrum analyzer when the locking was on and off. When the locking was on, the noise within 50 kHz bandwidth from the carrier was largely reduced.

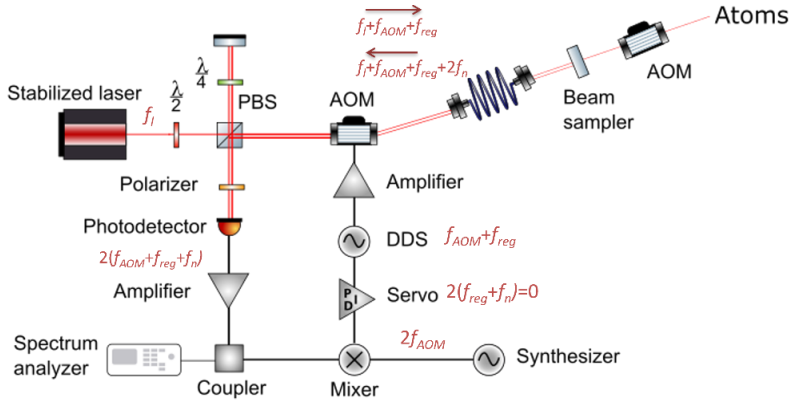

Fig. 2.17. The experimental setup of the fiber noise cancellation.

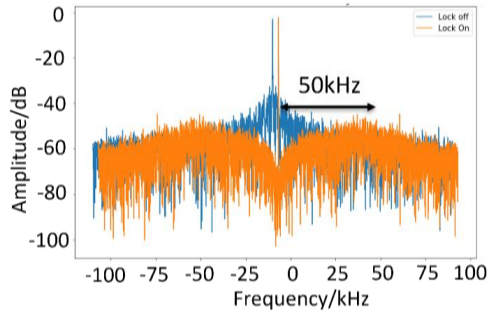

Fig. 2.18. The fiber noise compression result, the loop has a bandwidth of 50 kHz. The blue curve is when the lock was off and the orange curve is when the lock was on. The two curves were shifted against each other for clear display.

2.3. Conclusions and Future Work

Ultra-stable lasers are essential components in most of the quantum systems. In this chapter, we introduced the Pound-Drever-Hall technique and phase offset locking technique for laser stabilization. Two high-finesse cavities, vertical and horizontal, were utilized to lock a total of three external cavity diode lasers, including two clock lasers at 698 nm and a red MOT laser at 689 nm. The cavities were vibration and temperature isolated from the environment. The other red MOT laser was phase-offset locked to the stabilized laser operating at the same wavelength, offering a fast switch between ^{87}Sr and ^{88}Sr clocks.

The clock laser locked to the vertical cavity was beat against a commercial ultra-stable laser, the measured linewidth of the beat note signal was 161±50 Hz. To characterize the linewidth of each laser, in the next step, a commercial frequency comb being stabilized to the hydrogen maser will be installed in the same lab. The Three-Cornered Hat measurement will be performed among three independent oscillators: the lab constructed clock laser, the commercial ultra-stable laser, and the frequency comb. The stability and performance of each oscillator can be quantitatively determined.

By stabilizing the red MOT lasers to the horizontal cavity, we had attained primary results in the development of the ^{88}Sr clock: 35 % transition efficiency from the first stage cooling to the broadband red MOT was observed. The stabilization systems will be optimized further in the following months, to attempt the single-frequency second stage cooling and clock spectroscopy of ^{88}Sr and ^{87}Sr atoms.

A fiber noise cancellation setup was developed for precise dissemination of the ultra-stable lasers, the locking loop had a bandwidth of 50 kHz which significantly reduced the phase noise induced by the long fiber. This setup is portable and can be easily integrated into any laser distribution system that needs to be disseminated.

Acknowledgements

The authors would like to thank EPSRC, the UK Research and Innovation (project number 133976), the European Union's Horizon 2020 research and innovation program under grant agreement No 820404 (iqClock project), the Centre for Innovation in Advanced Measurement in Manufacturing (CIAMM), and UK Quantum Technology Hub Sensors and Timing (EP/T001046/1). The ComponentLibrary by Alexander Franzen which is licensed under a Creative Commons Attribution-NonCommercial 3.0 Unported License is also acknowledged for providing the optics drawing toolbox.

References

[1]. E. Cartlidge, Better Atomic Clocks Herald New Era of Timekeeping, *American Association for the Advancement of Science*, 2018.

[2]. M. Gellesch, J. Jones, R. Barron, A. Singh, Q. Sun, K. Bongs, *et al.*, Transportable optical atomic clocks for use in out-of-the-lab environments, *Advanced Optical Technologies*, Vol. 9, 2020, pp. 313-325.
[3]. Y. Wang, X. Lu, B. Lu, D. Kong, H. Chang, Recent advances concerning the 87Sr optical lattice clock at the national time service center, *Applied Sciences*, Vol. 8, 2018, 2194.
[4]. A. D. Ludlow, The Strontium Optical Lattice Clock: Optical Spectroscopy with Sub-Hertz Accuracy, *University of Colorado at Boulder*, 2008.
[5]. A. Franzen, ComponentLibrary, http://www.gwoptics.org/ ComponentLibrary/
[6]. R. Drever, J. L. Hall, F. Kowalski, J. Hough, G. Ford, A. Munley, *et al.*, Laser phase and frequency stabilization using an optical resonator, *Applied Physics B*, Vol. 31, 1983, pp. 97-105.
[7]. T. Kessler, C. Hagemann, C. Grebing, T. Legero, U. Sterr, F. Riehle, *et al.*, A sub-40-mHz-linewidth laser based on a silicon single-crystal optical cavity, *Nature Photonics*, Vol. 6, 2012, pp. 687-692.
[8]. J. Alnis, A. Matveev, N. Kolachevsky, T. Udem, T. Hänsch, Subhertz linewidth diode lasers by stabilization to vibrationally and thermally compensated ultralow-expansion glass Fabry-Pérot cavities, *Physical Review A*, Vol. 77, 2008, 053809.
[9]. S. Webster, M. Oxborrow, P. Gill, Vibration insensitive optical cavity, *Physical review A*, Vol. 75, 2007, 011801.
[10]. S. Johnson, Narrow Linewidth Lasers for Use with Neutral Strontium as a Frequency Standard, *University of Birmingham*, 2013.
[11]. C. Baynham, Digital Temperature Controller, https://github.com/ charlesbaynham/DigitalTemperatureController
[12]. G. Francois, F. Librecht, J. Engelen, Mode matching with a single thin lens, *Applied Optics*, Vol. 10, 1971, pp. 1157-1159.
[13]. S. Viswam, Advanced laser frequency stabilisation systems for mobile strontium optical lattice clocks, University of Birmingham, 2020.
[14]. E. D. Black, An introduction to Pound-Drever-Hall laser frequency stabilization, *American Journal of Physics*, Vol. 69, 2001, pp. 79-87.
[15]. J. C. Livas, J. I. Thorpe, K. Numata, S. Mitryk, G. Mueller, V. Wand, Frequency-tunable pre-stabilized lasers for LISA via sideband locking, *Classical and Quantum Gravity*, Vol. 26, 2009, 094016.
[16]. S. Zhang, Y. Singh, K. Bongs, Phase offset locking of 689 nm laser for the cold Sr atoms, in *Proceedings of the Conference on Lasers and Electro-Optics (CLEO'20)*, 2020, pp. 1-2.
[17]. A. Rönnholm, Fiber noise cancellation, in Lund Reports in Atomic Physics, *Lund University*, 2012.